Flow Turbulence Combust (2010) 85:397–419
DOI 10.1007/s10494-010-9288-x

Fractal-Generated Turbulence in Opposed Jet Flows

Philipp Geipel · K. H. Henry Goh · R. Peter Lindstedt

Received: 15 December 2009 / Accepted: 20 July 2010 / Published online: 17 August 2010

Abstract The opposed jet configuration presents a canonical geometry suitable for the evaluation of calculation methods seeking to reproduce the impact of strain and re-distribution on turbulent transport in reacting and non-reacting flows. The geometry has the advantage of good optical access and, in principle, an absence of complex boundary conditions. Disadvantages include low frequency flow motion at high nozzle separations and comparatively low turbulence levels causing bulk strain to exceed the turbulent contribution at small nozzle separations. In the current work, fractal generated turbulence has been used to increase the turbulent strain and velocity measurements for isothermal flows are reported with an emphasis on the axis, stagnation plane and the distribution of mean and instantaneous strain rates. Energy spectra were also determined. The instrumentation comprised hot-wire anemometry and particle image velocimetry with the flows to both nozzles seeded with 1 μm silicon oil droplets providing a relaxation time of $\simeq 3$ μs. It is shown that fractal grids increase the turbulent Reynolds number range from 48–125 to 109–220 for bulk velocities from 4 to 8 m/s as compared to conventional perforated plate turbulence generators. Low frequency motion of the order 10 Hz could not be completely eliminated and probability density functions were determined for the location of the stagnation plane. Results show that the fluctuation in the position of the stagnation plane is of the order of the integral length scale, which was determined to be 3.1 ± 0.1 mm at the nozzle exits through the use of hot-wire anemometry. Flow statistics close to the fractal plate located upstream of the nozzle exit were also determined using a transparent glass nozzle.

Keywords Opposed jets · Fractal grids · Inflow · Turbulent · PIV

Submitted for the Special Issue dedicated to S.B. Pope.

P. Geipel · K. H. H. Goh · R. P. Lindstedt (✉)
Department of Mechanical Engineering, Imperial College London,
South Kensington Campus, London SW7 2AZ, UK
e-mail: p.lindstedt@imperial.ac.uk

1 Introduction

Opposed jet geometries have been used extensively to study isothermal and combusting laminar and turbulent flows. For example, impinging flows have been used to evaluate calculation methods featuring cubic eddy viscosity approximations [1], second moment closures [2] and Large Eddy Simulations (LES) [3]. Lindstedt et al. [2] used the geometry to evaluate the generality of modifications to the dissipation rate equation based on the ratio of the turbulent to mean strain time scale, proposed by Yakhot et al. [4], alongside the Reynolds stress closure of Haworth and Pope [5, 6]. The configuration has also been proposed as a critical benchmark for combustion LES [7] as well as for moment based methods [8]. The focus of the current paper is on the measurement of velocity statistics inside and between two nozzles in an opposed jet geometry featuring enhanced turbulence generation and follows contributions by Rolon et al. [9], Mastorakos et al. [10], Kostiuk et al. [11], Mounaïm-Rousselle and Gökalp [12], Sardi et al. [13], Stan and Johnson [14], Geyer et al. [15] and, more recently, Coppola et al. [16] presented higher turbulence intensities in a opposed jet geometry using turbulence generators with a blockage of 90%.

The opposed jet geometry has the advantage of good optical access. Rolon et al. [9] used Laser-Doppler-Anemometry (LDA) to study the flow field of laminar non-reactive opposed jets and highlighted differences between the experimental flow field and the ideal flow case used in theoretical studies. It was shown that a constant velocity gradient along the axial and radial burner axis is present and the change of the axial and radial velocity profiles for various nozzle separations was quantified. Isothermal velocity field measurements were performed to understand the stagnating flow in the absence of combustion. Kostiuk et al. [11] measured the mean velocity and its fluctuations for a broad range of bulk velocities, nozzle separations and various turbulence intensities using Laser-Doppler-Velocimetry (LDV). The mean axial velocity profiles across the nozzle were assumed to be constant for the central region of the jets, as was the velocity gradient of the mean axial velocity at a distance of half a nozzle diameter from the stagnation point along the burner axis. Korusoy and Whitelaw [17] used static-pressure probes and measured a large static pressure increase at the nozzle exit plane for separations smaller than one nozzle diameter, which led to a decrease in axial mean velocity and also to increased values of the total strain rate along the stagnation point streamline. Lindstedt et al. [2] used Particle Image Velocimetry (PIV) to determine instantaneous velocity information and showed that the mean velocity profiles at the nozzle exit were increasingly less uniform when the nozzle separation was less than one nozzle diameter. Furthermore, an increase in the axial Reynolds stress component with higher bulk velocities was measured along the burner axis, while the radial component stayed unchanged.

A comparison of the Reynolds stresses presented by Lindstedt et al. [2], Kostiuk et al. [11] and Mastorakos [18] showed large discrepancies, possibly due to factors that include differences in burner design, turbulence intensities produced by the perforated plates, the distance between the turbulence generating plate and nozzle exit plane, the nozzle separation and bulk velocities. The different measurement techniques, Lindstedt et al. [2] used PIV whereas Kostuik et al. [19] and Mastorakos [18] used LDV, may also have contributed. A distinct advantage with

planar (e.g. PIV) measurements is that the stagnation plane can be located with much greater accuracy. Low frequency motion of the flow has been observed at high nozzle separations in several of the above studies (e.g. [12, 19]) and the comparatively low turbulence levels cause bulk strain to exceed the turbulent contribution at small nozzle separations. The current work is using fractal generated turbulence in order to increase the turbulent strain contribution and a more detailed analysis of the flow motion is also provided. The scaling and decay of fractal generated turbulence has been explored by Vassilicos et al. [20, 21] following the seminal analysis by Vassilicos and Hunt [22]. However, to our knowledge this is the first application of such grids in the context of opposed flows. Velocity statistics and strain rates obtained using PIV are presented with a focus on the burner centreline and the stagnation plane between the nozzles. Velocity measurements obtained using perforated plates, as used in earlier investigations by Lindstedt et al. [2], Mastorakos et al. [10], Kostiuk et al. [11], Sardi et al. [13] and Stan and Johnson [14], are also presented for comparison purposes.

The current work has implications for combusting flows. Flames in the opposed jet geometry are stabilised aerodynamically, thereby preventing all forms of heat loss other than radiation. Accordingly, flame dynamics and extinction are only related to aerodynamics, thermodynamics and the chemistry of the combustion process. The current fractal grids increase the turbulent Reynolds number range from 48–125 to 109–220 for bulk velocities from 4 to 8 m/s as compared to conventional perforated plates. The corresponding increase in the turbulent strain contribution is significant when compared to earlier studies of combusting flows, e.g. Geyer et al. [7], Lindstedt et al. [23], Kostiuk et al. [24], Mastorakos et al. [25] and Sardi et al. [26]. Furthermore, in-nozzle flow statistics were obtained close to the fractal plate through the use of a transparent glass nozzle in order to provide boundary conditions for computational studies. Finally, while the low frequency motion of the order 10 Hz could not be completely eliminated, probability density functions for the location of the stagnation plane were determined and show the movement to be of the order of the integral length scale of turbulence.

2 Experimental Configuration, Techniques and Uncertainties

The current opposed jet geometry consists of two identical nozzles in a vertical arrangement as designed by Geyer et al. [7, 15]. The outlet of each nozzle is 30 mm in diameter (D) and in the basic configuration (e.g. [7]) turbulence is generated 50 mm upstream of the nozzle exit plane using perforated plates with a hole diameter of 4 mm and a blockage of 45% as also used by Lindstedt et al. [2, 23], Mastorakos et al. [10, 25, 27] and Sardi et al. [13, 26, 28]. The distance between the two nozzles could be varied by moving the lower nozzle. If not stated otherwise, the nozzle separation (H) was set to one nozzle diameter (H/D = 1) following the extensive studies by Luff [29], which showed that the radial velocity profile along the nozzle exit became increasingly non-uniform for nozzle separations below one diameter. Greater radial acceleration beyond a distance of 1.0D for the stagnation plane was also found with a reduction in nozzle separation. Korusoy and Whitelaw [17] also

showed that the mean position of the stagnation point drifted axially with nozzle separations H/D $\geq$ 2.

To increase the turbulence intensities at the nozzle exits, fractal grids were introduced in addition to the perforated plates. Fractal-generated turbulence has been studied by Vassilicos et al. [20–22] and shown to exhibit interesting characteristics such as enhanced turbulence generation. Fractal grids suitable for the current opposed jet geometry were designed and, following a preliminary investigation, a parametric study of five different fractal cross grids was performed. The fractal grids were located 10 mm downstream of the perforated plates. A schematic of the top nozzle is presented in Fig. 1, which highlights the location of the fractal grids, and the tested plates are shown in Fig. 2. The details of the parametric variations are discussed below.

A particle image velocimetry system (LaVision Flowmaster 3) was used to measure the axial and radial velocity components. The central plane perpendicular to the nozzle exits was illuminated by two 120 mJ Solo-New Wave double pulse Nd:YAG lasers. The laser head was equipped with LaVision light sheet optics which allowed an adjustable light sheet thickness between 0.5 mm and 2.5 mm with the value set to $\simeq$ 0.8 mm for all measurements presented. The flow field was viewed using a 12 bit, 10 Hz CCD Imager Intense camera equipped with a 50 mm Nikon lens. For each correlation, two images of 1,376 $\times$ 1,040 pixel were divided into smaller interrogation windows, each with the size N $\times$ N $= 2^i$ pixels (here $i = 5$, 6 and 7). Thus a decreasing window size was chosen starting from 128 $\times$ 128, via 64 $\times$ 64 down to 32 $\times$ 32 pixels with a 50% overlap, leading to a vector spacing of 0.4 mm. The time between the two

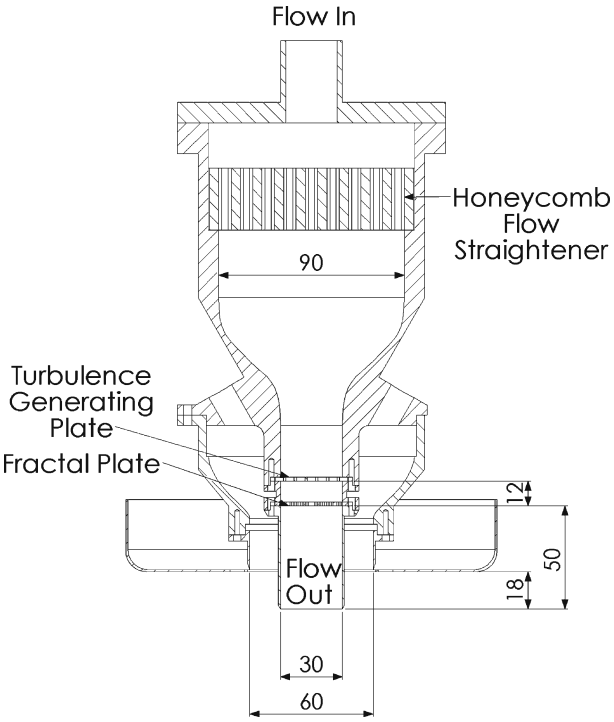

Fig. 1 Schematic of the upper nozzle of the opposed jet geometry

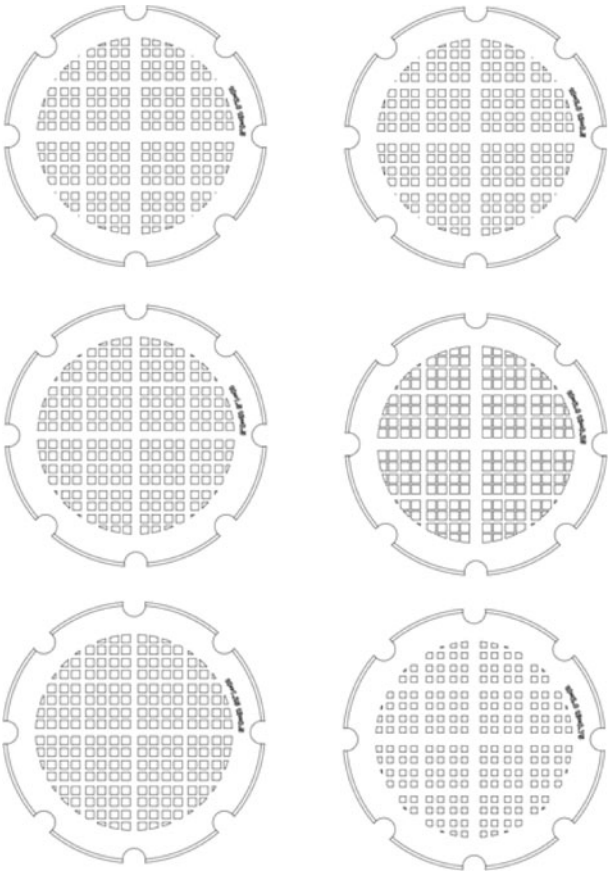

Fig. 2 Schematics of the fractal cross grids used in the parametric study. Grid I (*top left* and *top right*), Grid II (*middle left*), Grid III (*bottom left*), Grid IV (*middle right*) and Grid V (*bottom right*). *Left column* corresponds to the results shown in Fig. 4 and the *right column* to the results shown in Fig. 5. Grid I was used to produce the results shown in all subsequent graphs

PIV-images was adjusted between 15–50 μs according to the nozzle separation and the mean bulk velocity in order to reduce spurious vectors. All velocity and strain rate data was obtained by averaging 1,000 (statistically independent) instantaneous vector fields using a purpose written FORTRAN program.

For all flow measurements dry and filtered air was supplied at 4 bar(g) by a compressor to each nozzle using digital mass flow controllers (Bronkhorst UK LTD). The accuracy deviation of each mass flow controller was $\leq$0.8% RD (reading) plus $\leq$0.2% FS (full scale) and the reproducibility error $\leq$0.1%. The mass flow rate was monitored using a custom written LabView interface connected to a Readout/Control Unit Type E-7000 that was connected via a flow-bus system to each of the four air mass flow controllers. This allowed more accurate control of each mass flow rate and ensured the desired bulk flow velocity. A bulk velocity range of 4.0 m/s to 8.0 m/s, corresponding to Reynolds numbers in the range 7,800–15,500, was covered. The corresponding turbulent Reynolds numbers were 48–125 for the standard perforated plate configuration and 109–220 for the selected fractal grid (Grid I).

A co-flowing stream of air with a velocity of 30% of the corresponding bulk flow velocity was used for each measured flow condition. The co-flow was used to

reduce the effect of the shear layer that forms between the opposed jet flows and the ambient air. The effects were investigated by Mounaïm-Rouselle and Gökalp [12], who considered the appearance, location and stability of flames in a counterflow geometry and the influence of a co-flowing stream. Kostiuk et al. [19, 30] stated that at larger separations an axial movement of the flow at a low frequency was observed resulting in a bouncing of the flame brush. A stabilisation of the flame brush off the symmetry plane of the burner was also noticeable. In the current work, such effects were minimised by co-flowing streams with the flow rates controlled by two rotameters (Rotameter-KDG Instruments) with an accuracy of 2.5% of full scale deflection giving an overall error of less than 5%.

The seeding of the flow was obtained by silicon oil droplets 1 μm in diameter produced using two PALAS Aerosol Generators Type AGF 10.0. The mass flow through each seeder was controlled by a separate mass flow controller to ensure equal seeding densities for both nozzles. The main air flow and the secondary stream carrying the seeding particles were mixed over a length of approximately 1 m before entering each nozzle. Stagnating flows have a high dynamic range ($U_{\max}/U_{\min}$) with the minimum velocity approaching zero at the stagnation plane where the largest measurement errors can be expected as discussed by Lindstedt et al. [23]. The relaxation time of a seeding particle to a step change in the fluid velocity was estimated using the approach of Han and Mungal [31] and the value of $\simeq 3$ μs obtained for the current silicon oil seeding is sufficient for particle lag not to influence the current measurements.

In order to obtain energy spectra and lengthscale information flow measurements were also performed using a *DANTEC* streamline flow unit in order to obtain instantaneous axial velocities 1.5 mm downstream of the top nozzle. A single 5 μm platinum coated tungsten wire, calibrated in a *DANTEC* frame unit, was traversed radially from the centreline of the nozzle to a radius of 13 mm using 1 mm steps. A sampling frequency of 20 kHz was chosen, which resulted in an effective spatial resolution of 0.2 mm for a bulk velocity of 4.0 m/s. A 20-point fitted calibration curve was calculated for the velocity measurements taking temperature compensation into account, while mounting the hot wire probe in the test rig great care was taken to ensure it had the same orientation as in the calibration unit. PIV measurements at different resolutions were also performed inside the nozzles in order to determine the energy spectrum with the data compared to hot-wire measurements taken on the burner axis for a single nozzle at a position 15 mm upstream of the nozzle exit.

3 Results

Fractal-generated turbulence was introduced 50 mm upstream from the nozzle exit by 2 mm thick grids as shown in Fig. 1. A fractal dimension (D_f) of 2.0 for space filling cross grids, as suggested by Hurst and Vassilicos [20], was used and five different grids were selected for a parametric study. The applied grid parameters are shown in Table 1, where δ is the blockage of the grids with $T_{\max}$ the largest and $T_{\min}$ the smallest fractal bar width. Drawings used for the manufacture of the tested grids are shown in Fig. 2. In the discussion below, the distance from the fractal grid is denoted x_G while the distance from the nozzle exit is given as x.

Table 1 Parameters for the fractal cross grids

Grid type	Blockage (δ)	T_{max} [mm]	T_{min} [mm]
I	65%	2.0	0.5
II	60%	1.5	0.5
III	57%	1.25	0.5
IV	50%	2.0	0.25
V	77%	2.0	0.75

In order to measure flow statistics close to the fractal plate, the steel nozzle of the lower jet was replaced by a glass nozzle with equal dimensions. Measurements of velocity inside the nozzle were obtained in order to understand the flow field evolution and to provide boundary conditions for computational studies. The axial

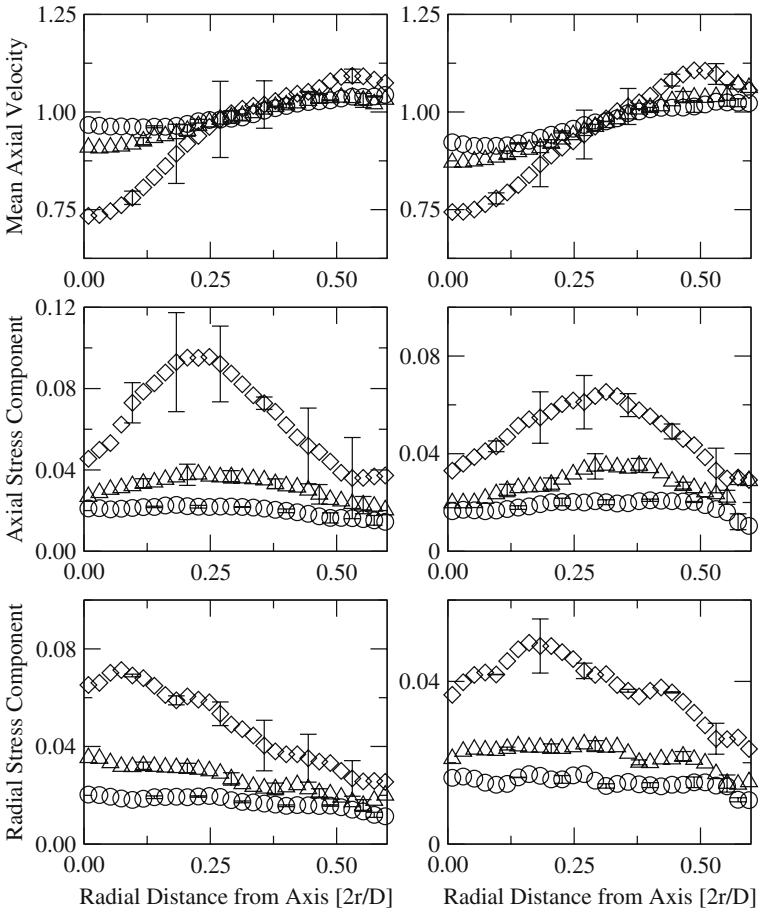

Fig. 3 The axial development of the flow field inside the nozzle downstream of Grid I as shown in Fig. 2. *Left* $U_b = 4.0$ m/s and *right* $U_b = 8.0$ m/s. *Upper row* normalised mean axial velocity, *middle row* normalised axial Reynolds stress component and *lower row* radial Reynolds stress component. $\diamond$ 0.7 x_G/D; $\triangle$ 1.0 x_G/D; and $\circ$ 1.3 x_G/D. The nozzle exit is located at x_G/D = 1.67

development of the flow inside the nozzle behind Grid I is shown at three locations (x_G/D = 0.7, 1.0 and 1.3) in Fig. 3 and for bulk velocities of 4 and 8 m/s. The vertical bars shown indicate the sum of all errors including those caused by flow asymmetry and the same applies to all subsequent graphs unless otherwise stated. The results show that an essentially uniform flow field is achieved before the nozzle exit at x_G/D = 1.67 is reached.

Results obtained for other fractal grids with variations of the largest and smallest fractal widths can be found in Figs. 4 and 5. Again the mean radial velocity profiles corresponding to bulk velocities of 4.0 and 8.0 m/s are shown along with normalised Reynolds stress components at 4.0 m/s. The axial location corresponds to 10 mm upstream of the nozzle exit (x_G/D = 1.3). Mean velocity profiles show a reduction close to the centre of the grid where the largest fractal cross is located. The drop in the mean velocity reduces with an increase in the total blockage of the grid. The grid with a width of 2.0 mm for the largest bar provided the highest turbulent intensities and the most isotropic flow conditions as shown in the lower half of Fig. 4. The variation of the smallest bar width and its influence on the mean axial velocity profiles and their fluctuations is shown in Fig. 5.

The mean profiles obtained for bulk velocities of 4.0 and 8.0 m/s show an increase in homogeneity as the blockage is increased to 77% of the total area—in agreement with the findings shown in Fig. 4. The Reynolds stresses shown in the lower half of Fig. 4 suggest higher intensities with an increase of the width, and hence the blockage ratio, of the smallest grid bar. However, as the blockage ratio goes above 65%, the

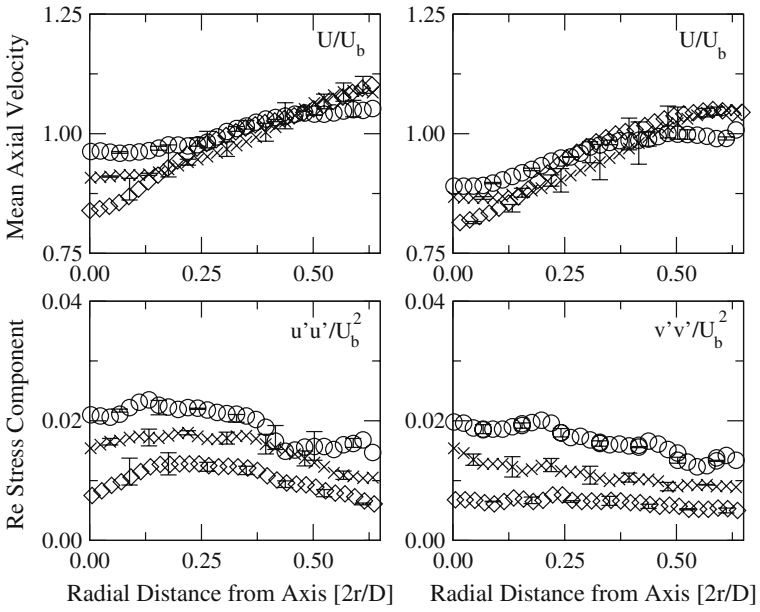

Fig. 4 Variation of the largest fractal width (T_{max}) at constant T_{min} of 0.5 mm. *Upper row* normalised mean bulk velocity. *Left* U_b = 4.0 m/s and *right* U_b = 8.0 m/s. *Lower row* normalised axial (*left*) and radial (*right*) Reynolds stress components at U_b = 4.0 m/s. ∘ T_{max} = 2.0 mm; × T_{max} = 1.5 mm and ⋄ T_{max} = 1.25 mm. The axial location corresponds to 10 mm upstream of the nozzle exit (x_G/D = 1.3)

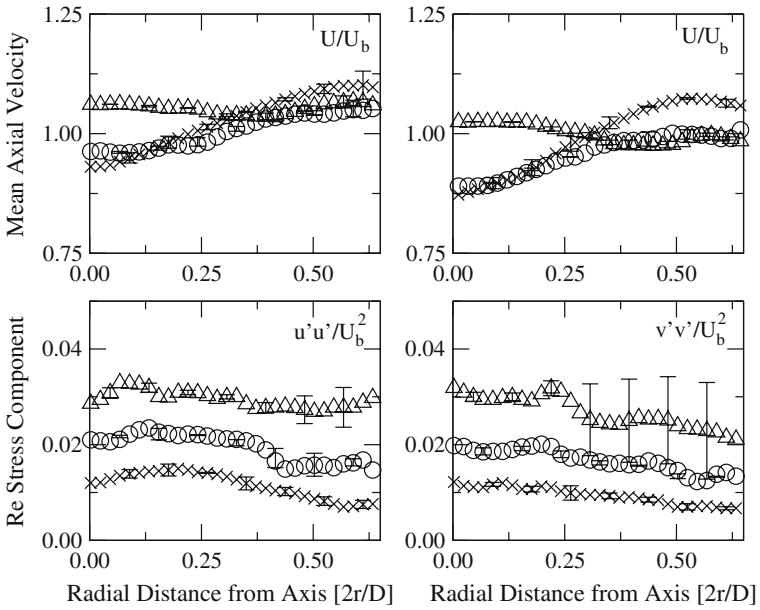

Fig. 5 Variation of the smallest fractal width ($T_{\min}$) at constant $T_{\max}$ of 2.0 mm. *Upper row* normalised mean bulk velocity. *Left* $U_b = 4.0$ m/s and *right* $U_b = 8.0$ m/s. *Lower row* normalised axial (*left*) and radial (*right*) Reynolds stress components at $U_b = 4.0$ m/s. $\triangle$ $T_{\min} = 0.75$ mm; $\circ$ $T_{\min} = 0.5$ mm and $\times$ $T_{\min} = 0.25$ mm. The axial location corresponds to 10 mm upstream of the nozzle exit (x_G/D = 1.3)

radial stress becomes less uniform despite errors smaller than 0.5° in the angular alignment of each nozzles. The effect also becomes noticeable in the mean velocities and axial fluctuations. Overall, the optimal blockage fraction for the fractal cross grids is between 65 and 77%. However, the strong sensitivities noted at very high blockage ratios can be expected to impact reproducibility of results and, accordingly, the fractal grid with the dimensions shown as Grid I in Table 1 was chosen for all remaining measurements. Contour plots of the mean axial velocity and the axial and radial Reynolds stress components at a distance between 10 and 40 mm downstream of Grid I are shown in Fig. 6. The above discussion suggests that, while the blockage ratio is a key parameter, the dimensions of the fractal grids can be used to "tailor" turbulence characteristics to some extent.

A reduction in the mean axial velocities can be found close to the burner axis due to the influence of the largest fractal cross. The mean axial velocity profile becomes more homogenous with an increase in distance from the fractal grid. A degree of inhomogeneity is noticeable at the nozzle exit plane (also see Fig. 10 and discussion below). The highest axial Reynolds stresses are found in the region of second largest fractal cross, whereas the radial stress component shows a less distinct maximum. Both Reynolds stress components homogenise towards the nozzle exit to a value of approximately 0.025 U_b^2. As also shown in Fig. 5, the flow 10 mm upstream of the nozzle exit is close to isotropy. Hence, the evolution of the flow field moves from anisotropy close to the fractal grid via more homogeneous conditions before leading to anisotropy towards the stagnation plane as discussed below.

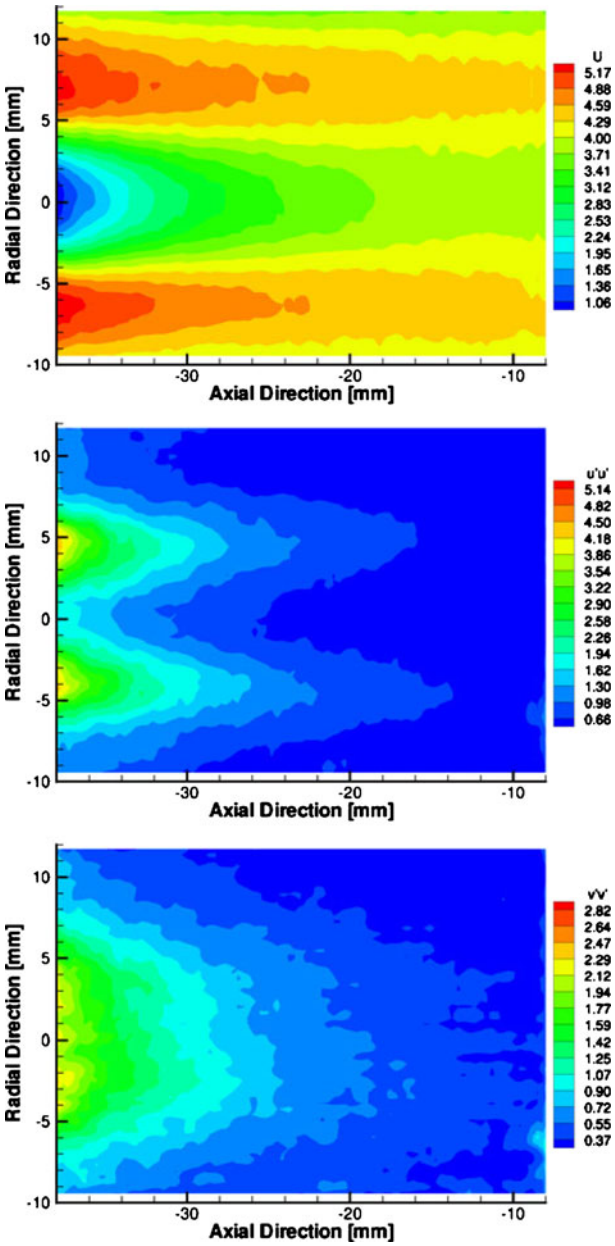

Fig. 6 Contours of mean axial velocities (*upper*), axial (*middle*) and radial (*lower*) Reynolds stress components upstream of the nozzle exit plane obtained with Grid I. The velocity statistics shown represent the flow upstream of the nozzle exit plane and were measured using a glass nozzle. The burner axis is located at 0 mm in radial direction, whereas a value of −50 mm in axial direction would denote the location of the fractal grid and 0 mm the nozzle exit plane

3.1 Mean velocities and normal stresses

A low frequency bulk motion in the axial direction has been reported by Rolon et al. [9], Deshchikov et al. [32, 33] and Mounaïm-Rousselle and Gökalp [34] among others. In the current work the effect was noticeable and could not be fully eliminated

by the use of a co-flowing stream of air. Probability density functions for the instantaneous location of the stagnation point were obtained for bulk velocities of 4.0 and 8.0 m/s and are shown in Fig. 7. It was found that the instantaneous stagnation point moves approximately 4 mm in axial direction and up to 2 mm in the radial direction for the 4.0 m/s case. The scale of the movement is similar to the integral length scale of turbulence which for the latter velocity was determined to be 3.1 ± 0.1 mm through the use of hot wire anemometry. It can also be seen that at higher bulk velocities the radial movement is reduced to around 1 mm.

Two algorithms were developed to trace the location of the stagnation point from each instantaneous vector field obtained using PIV. The first algorithm defined the stagnation point as the location of the velocity vector with the lowest magnitude along the burner axis. The second algorithm used a square window of fixed size. The centre of the window was moved around each PIV frame and a vector summation of the velocities computed. The location of the instantaneous stagnation point was then defined as the centre of the window with the lowest magnitude of the vector sum. The width of the interrogation window was varied from 2 to 50 times the vector spacing. It was found that as the window size increased, the location of the stagnation point converged with an average deviation of less than 0.25 mm for vector spacings in excess of 30 as shown in Fig. 8. All subsequent calculations using this algorithm featured a window size of 36 times the vector spacing of the corresponding PIV frame.

The two algorithms were compared by overlaying the calculated positions of the instantaneous stagnation point on the velocity field for each PIV frame. The procedure showed that the first algorithm, which calculates the lowest magnitude of the velocities along the burner centreline, failed whenever large scale eddies were present in the flow as it identified the centre of the eddy as the stagnation point. Furthermore, it failed to detect the stagnation point when it was not present along the centreline. The latter limitation is also significant for the current range of bulk velocities as shown in Fig. 7. The second algorithm, which considered an area rather than a line, was able to detect the location of the instantaneous stagnation point for all measured flow velocities.

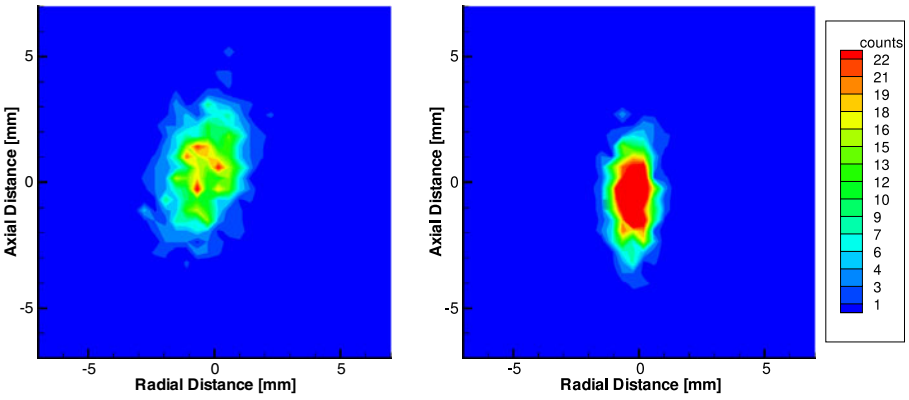

Fig. 7 Probability density functions of the instantaneous stagnation point for bulk velocities of 4.0 m/s (*left*) and 8.0 m/s (*right*)

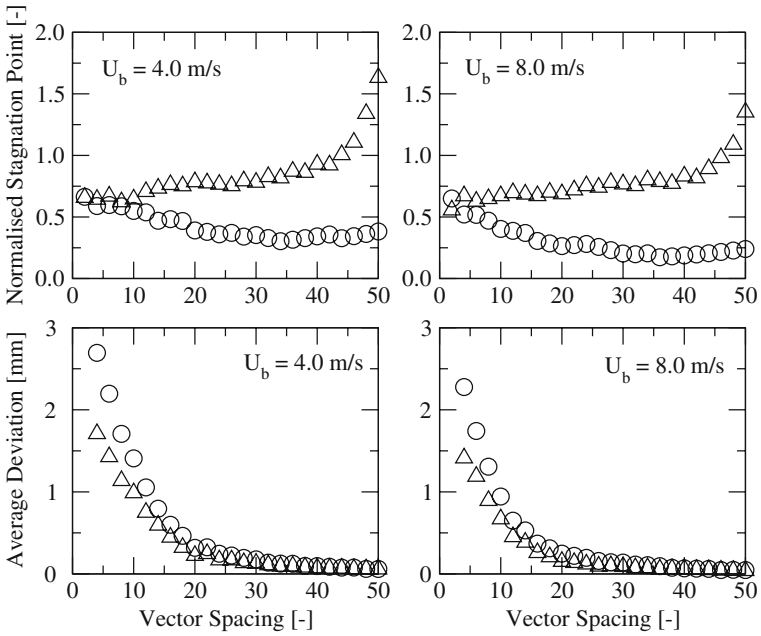

Fig. 8 Effects of increasing window size on locations of the stagnation points. *Upper row* locations of the furthest instantaneous stagnation point from the nominal stagnation point position in radial and axial directions. Normalised against the maximum location of the algorithm. *Lower row* average deviations of stagnation point as window size increases. ○ radial direction, △ axial direction. *Left* U_b = 4.0 m/s, *right* U_b = 8.0 m/s

The movement of the stagnation point can contribute to the measured Reynolds stress components. Accordingly, the impact of axial thresholds for the permitted maximum movement away from the nominal stagnation point location was assessed. It is important to note that the rejection of an excessive number of PIV frames will result in excessive statistical errors. The impact on the measured turbulence velocities was assessed by introducing thresholds for the maximum allowed movement in steps of 0.5 mm and covering the range from 0.0 to 10.0 mm. The number of rejected frames and the corresponding impact on velocity statistics was also recorded. A number of bulk velocities in the range 4.0 and 8.0 m/s were analysed.

An axial threshold of 5 mm included all measured velocity vector fields as the maximum movement of the instantaneous stagnation point was limited to 4 mm from the nominal centre point. Reducing the threshold by 50% to 2.5 mm, which is close to the integral length scale of the flow (3.1 ± 0.1 mm), reduced the peak axial Reynolds stress by $0.01\ U_b^2$ and also led to a narrower profile as shown in Fig. 9. The threshold resulted in a rejection of 12% of the frames at a bulk velocity of 4.0 m/s and 7% at 8.0 m/s. Decreasing the threshold to 1 mm caused an arguably unacceptable rejection of almost 50% of the PIV frames and resulted in a loss of symmetry of the axial Reynolds stress component with a further significant impact on the peak value. However, it seems questionable to impose a criteria demanding a movement less than the integral length scale of turbulence. The radial Reynolds stress component was not strongly affected in either shape or magnitude. No movement threshold

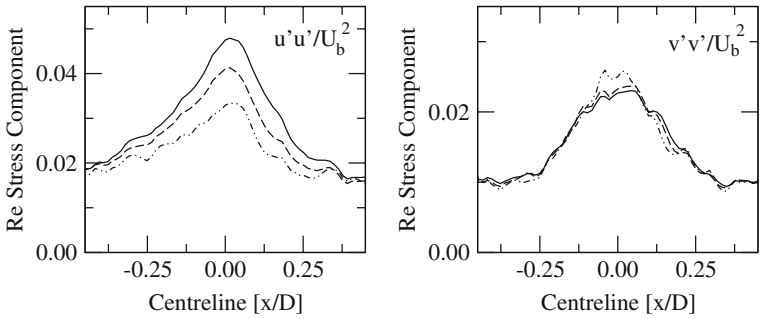

Fig. 9 Effect of an increasing axial threshold on the centreline profiles of the normalised axial (*left*) and radial (*right*) Reynolds stress components at a bulk velocity of $U_b = 4.0$ m/s. *Solid line* 5 mm, *dashed line* 2.5 mm and *dashed-dotted line* 1 mm axial threshold

was imposed on any of the results reported in the current study unless otherwise stated.

Mean velocity profiles 3.0 mm downstream of the nozzle exit are shown in the upper half of Fig. 10 for both perforated plates and fractal grids. A large reduction in the mean axial velocity to approximately 0.8 U_b is observed at the centreline when the fractal grid is used. The mean axial velocity profile obtained with the perforated plates shows greater uniformity at the expense of some asymmetry. The

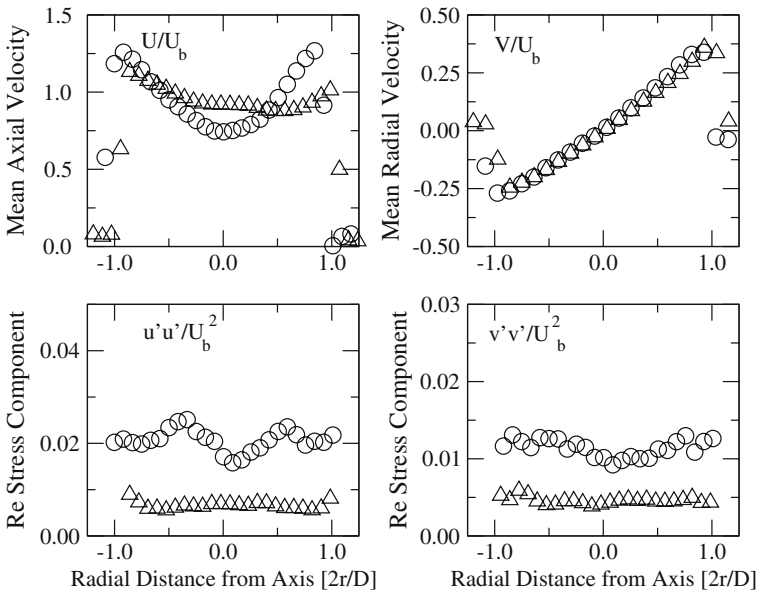

Fig. 10 Comparison of the perforated plates with 4.0 mm holes and fractal Grid I. *Upper row*, *left* normalised axial and *right* normalised radial velocity with $U_b = 4.0$ m/s at a distance of 3.0 mm from the nozzle exit. *Lower row* normalised Reynold stress components. △ perforated plate and ○ fractal grid

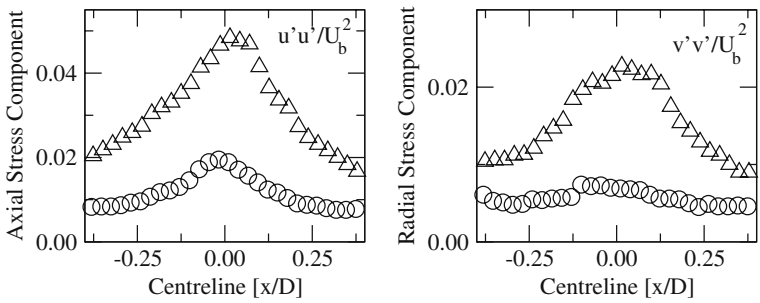

Fig. 11 Centreline profiles of the normalised axial (*left*) and radial (*right*) Reynolds stress components at a bulk velocity of $U_b = 4.0$ m/s. ○ represents the measurement using the perforated plates and △ the measurements with the addition of fractal Grid I

radial velocities are of comparable magnitude with the expected acceleration towards the nozzle rim. Turbulence intensities are increased by a factor of two with Grid I as can be seen for both Reynolds stress components in the lower half of Fig. 10. A certain degree of inhomogeneity is present along the nozzle diameter.

Normalised Reynolds stress components obtained with both nozzles fitted with either perforated plates or the fractal grids are shown in Fig. 11. An increase from 0.01 to 0.02 U_b^2 at both nozzle exits was found for axial and radial stress components along the centreline of the burner. The axial Reynolds stress component increased to 0.05 U_b^2 towards the nominal stagnation point of the flow, whereas the radial component increased to 0.025 U_b^2 for a bulk velocity of 4.0 m/s. The increase of the normal stresses was maintained for bulk velocities up to 8.0 m/s as shown in Fig. 12. Hence, the Reynolds stress components scale as a function of the bulk velocity for the considered velocity range. It may also be noted that the asymmetry of the flow reduced with an increase in the bulk velocity.

The influence of increasing nozzle separation on the mean velocities and the normal stresses was investigated 3.0 mm from the exit plane of the bottom nozzle by setting H/D = 1.0, 1.2 and 1.4 as shown in Fig. 13. Due to a decrease in the static

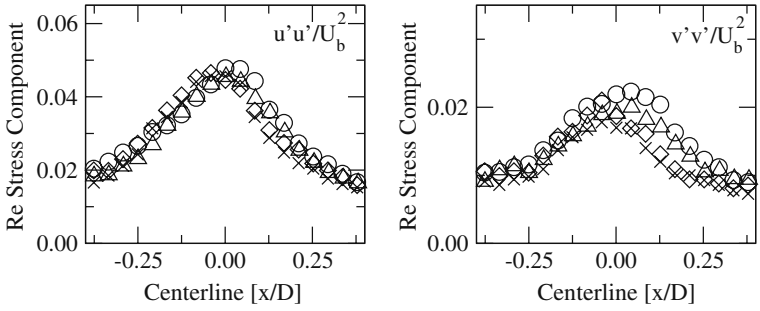

Fig. 12 The effects of increasing bulk velocity on the axial (*left*) and on the radial (*right*) normal stress component along the centreline with a bulk velocity of $U_b =$ ○ 4.0, △ 5.0, ◇ 6.0, and × 8.0 m/s. Fractal Grid I was used

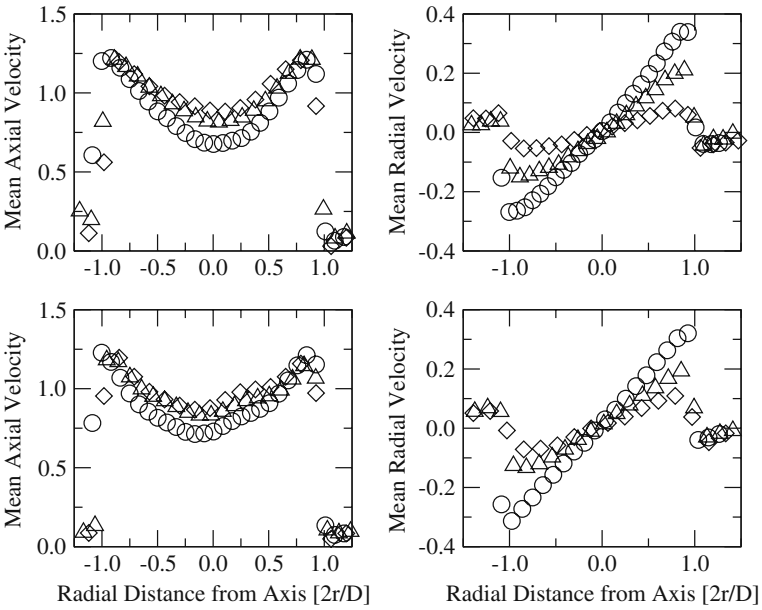

Fig. 13 The effects of increasing nozzle separation on mean velocities at 3.0 mm distance from the nozzle exit with bulk velocity of $U_b = 4.0$ m/s (*upper*) and $U_b = 8.0$ m/s (*lower*). *Left* normalised mean axial velocity. *Right* normalised mean radial velocity. H/D: ∘ 1.0, △ 1.2 and ⋄ 1.4

pressure at the axis with increasing nozzle separation, higher values of the mean axial velocity in the central area of the nozzle and lower values of the mean radial velocity towards the nozzle rim can be seen. With respect to the profiles at the stagnation plane, the largest change was found in the radial stresses. The latter reduce by $0.01U_b^2$ following an increase in nozzle separation to 1.4 H/D, as shown in Fig. 14, while all other quantities remain of comparable magnitude. The findings are in agreement with results presented by Lindstedt et al. [2] and Korusoy and Whitelaw [35].

3.2 Energy spectra

Hot-wire data obtained 1.5 mm downstream and 15 mm upstream of the nozzle exit was used to calculate one-dimensional energy spectra ($E_{11}(\kappa_1)$) through the longitudinal autocorrelation function ($f(r_1)$) shown in (1).

$$E_{11}(\kappa_1) = \frac{2}{\pi}\left\langle u_1^2 \right\rangle \int_0^\infty f(r_1)\cos(\kappa_1 r_1)dr_1 \tag{1}$$

A comparison of the measurements with the corresponding model spectrum suggested by Pope [36] (see (2–5)) is shown in Fig. 15. The constant C_L in (4) has a value of 6.78 at high Reynolds numbers [36]. Measured energy spectra obtained for the fractal grids were found to agree for $C_L \simeq 3$ as shown in Fig. 15, where a range of values ($1 \leq C_L \leq 6.78$) have been included. The impact of variations in C_η (see (5)) was found to be less prominent with changes mainly affecting the spectrum at higher

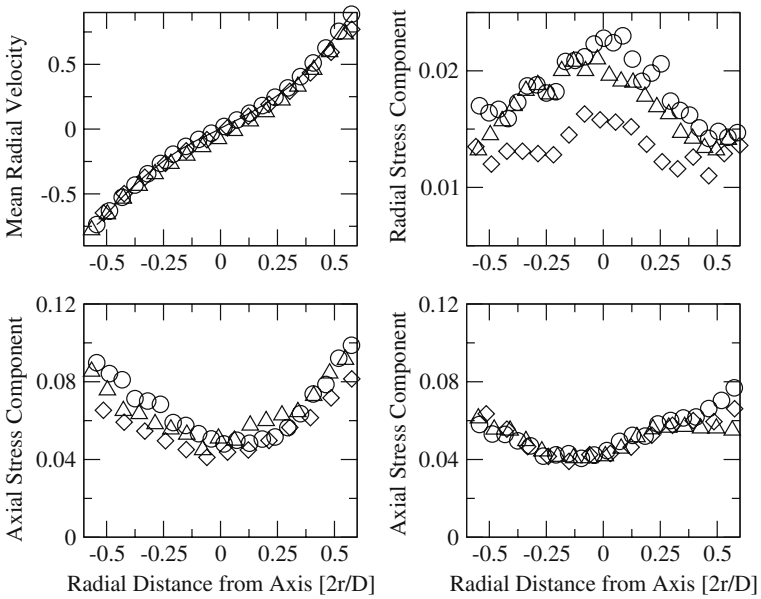

Fig. 14 The effect of increasing nozzle separation on the mean radial velocity and the Reynolds stress components along the nominal stagnation plane. *Upper row* mean radial velocity and radial stress component for $U_b = 4.0$. *Lower row* axial stress component for (*left*) $U_b = 4.0$ m/s and (*right*) $U_b = 8.0$ m/s. H/D: ∘ 1.0, △ 1.2 and ◇ 1.4

wavenumbers and the standard value of 0.4 was retained. Further comparisons of the measurements with the von Kármán [37], exponential [38] and Pao [39] spectra are also shown in Fig. 15. All parameters used can be found in Table 2 [36]. Experimental noise influences the measured spectra at high wavenumbers. However, the measured and calculated energy spectra agree reasonably well for $\kappa_1\eta \leq 0.09$. The exception is

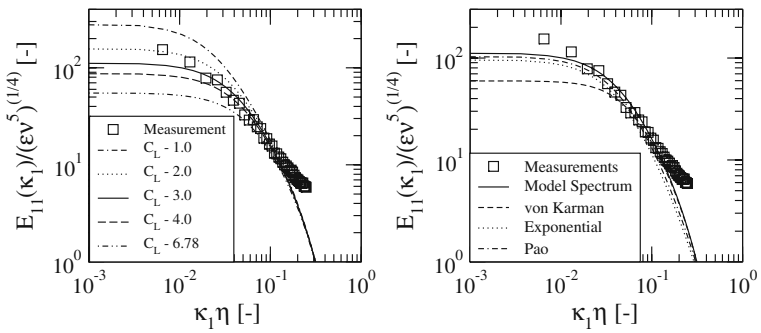

Fig. 15 *Left* comparison of the measured longitudinal velocity spectrum (*square*) obtained using hot-wire anemometry with the model spectrum (2) for different values of C_L. *Right* longitudinal velocity spectra for the model (*solid line*), von Kármán (*dashed*), exponential (*dotted*) and Pao spectra (*dashed-dotted*) obtained using $C_L = 3.0$ and compared with experimental data (*square*) obtained using the fractal-grids

Table 2 Measured data and parameters taken from Pope [36] and used in (4) and (5) to calculate the energy spectra (E_{11}) shown in Figs. 15 and 16

Constant	Model-spectrum	von Kármán	Exponential	Pao
p_0	2	4	2	2
C_L	3	3	3	3
C_η	0.4	0.4	0.4	0.4
β	5.2	5.2	5.2	5.2
C	1.5	1.5	1.5	1.5
ε_1 [m^2s^{-3}]	42.2	42.2	42.2	42.2
η_1 [mm]	$9.51{\cdot}10^{-2}$	$9.51{\cdot}10^{-2}$	$9.51{\cdot}10^{-2}$	$9.51{\cdot}10^{-2}$
ε_2 [m^2s^{-3}]	44.3	44.3	44.3	44.3
η_2 [mm]	$9.39{\cdot}10^{-2}$	$9.39{\cdot}10^{-2}$	$9.39{\cdot}10^{-2}$	$9.39{\cdot}10^{-2}$
ε_2[a] [m^2s^{-3}]	49.1	49.1	49.1	49.1
η_2[a] [mm]	$9.16{\cdot}10^{-2}$	$9.16{\cdot}10^{-2}$	$9.16{\cdot}10^{-2}$	$9.16{\cdot}10^{-2}$

[a] l_t was determined using hot-wire data and k using PIV measurements

the von Kármán spectrum, which underestimates the energy at lower wavenumbers. The model spectrum provides the best agreement and was chosen for subsequent comparisons.

$$E_{11}(\kappa_1) = \int_{\kappa_1}^{\infty} \frac{E(\kappa)}{\kappa} \left(1 - \frac{\kappa_1^2}{\kappa^2} d\kappa\right) \tag{2}$$

$$E(\kappa) = C\varepsilon^{2/3}\kappa^{-5/3} f_L(\kappa L)\, f_\eta(\kappa\eta) \tag{3}$$

$$f_L(\kappa L) = \left(\frac{\kappa L}{\left[(\kappa L)^2 + C_L\right]^{1/2}}\right)^{5/3+p_0} \tag{4}$$

$$f_\eta(\kappa\eta) = \exp\left\{-\beta\left\{\left[(\kappa\eta)^4 + C_\eta^4\right]^{1/4} - C_\eta\right\}\right\} \tag{5}$$

The rate of dissipation (ε) was obtained from the measured energy decay rate (e.g. Comte-Bellot and Corrsin [40]) using (6) and also calculated using the approximation in (7), where l_t is the integral lengthscale of the flow measured using hot-wire anemometry. The value $l_t = 3.1$ mm was obtained for the fractal grids and $l_t = 2.6$ mm for the conventional perforated plates. The turbulent kinetic energy was obtained from hot-wire measurements and PIV-data as highlighted in Table 2. The values of the dissipation rate were found to be within 14% and (6) was used in the calculation of the energy spectra. Kolmogorov length scales were estimated using $\eta = (\nu^3/\varepsilon)^{1/4}$ with $\nu = 1.51 \cdot 10^{-5}$ m^2/s and are also shown in Table 2 for the different values of the dissipation rate.

$$\varepsilon_1 = -\frac{3}{2}\bar{U}\frac{d\overline{u'^2}}{dx} \tag{6}$$

$$\varepsilon_2 \simeq \frac{k^{3/2}}{l_t} \tag{7}$$

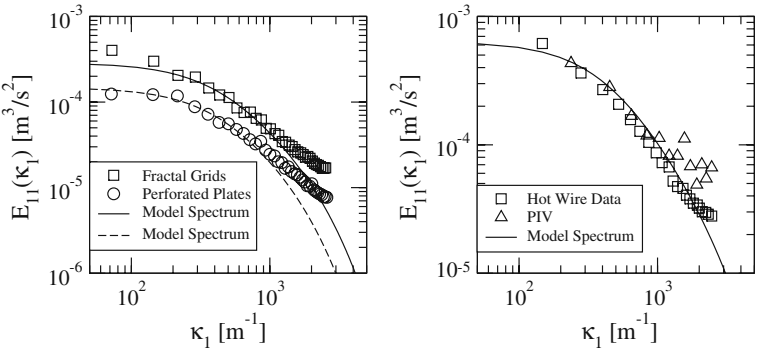

Fig. 16 *Left* comparison of the measured longitudinal energy spectra for the perforated plates (○) and fractal grids (*square*) at a distance of 1.5 mm downstream of the nozzle exit with model spectra (2). *Right* PIV data (△) at a medium resolution ($L = 4.6l_t$ and $L_w = 0.33$ mm), hot wire measurements (*square*) and the model spectrum (*solid line*) 15 mm upstream the nozzle exit for the fractal grids

Measured energy spectra obtained at a position 1.5 mm downstream of the centre of the nozzle exit plane for the conventional perforated plates and the fractal grids are shown in Fig. 16. It is apparent that the fractal grids produce higher energy levels over the whole wavenumber range. In case of the perforated plates, C_L was set to 2.0 in order to fit the model spectrum as compared to $C_L = 3.0$ used for the fractal grids. The decrease in C_L is consistent with the observed lower turbulent Reynolds numbers.

PIV data was also used to obtain the energy spectrum at a location 20 mm upstream of the nozzle exit as shown in Fig. 17. Three resolutions were used. A low resolution, here considered as an interrogation window size (L_w) $\simeq$ 0.4 mm (around four times the estimated Kolmogorov scale), and a domain length (L) $\simeq$ $6l_t$. The arrangement permits the resolution of a wavenumber range from $3 \cdot 10^2$ up to $2 \cdot 10^3$. A high resolution using $L_w \simeq 0.1$ mm, which is of the order of the Kolmogorov lengthscale, and $L \simeq 1.5l_t$ results in wavenumbers between 1.5 and

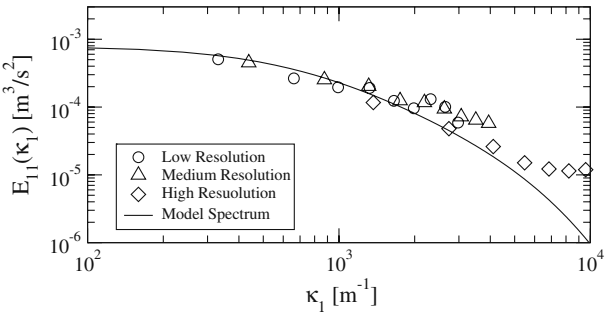

Fig. 17 The effect of different domain lengths (L) and interrogation window sizes (L_w) on measurements of the energy spectrum using PIV. Low resolution (○) with $L = 6.1l_t$ and $L_w = 0.42$ mm, medium resolution (△) with $L = 4.6l_t$ and $L_w = 0.33$ mm and high resolution (◇) with $L = 1.5l_t$ and $L_w = 0.09$ mm. The solid line is the standard model spectrum by Pope [36]

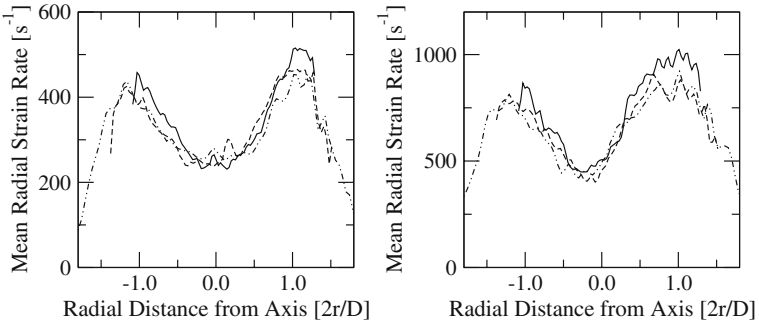

Fig. 18 Mean radial strain along the nominal stagnation plane with increasing nozzle separation. Bulk velocity of (*left*) 4.0 m/s and (*right*) 8.0 m/s. H/D: *solid line* 1.0, *dashed line* 1.2 and *dotted-dashed* 1.4

$5 \cdot 10^3$. The compromise between the domain length and interrogation window size is a limiting factor in the derivation of energy spectra using PIV measurements. A

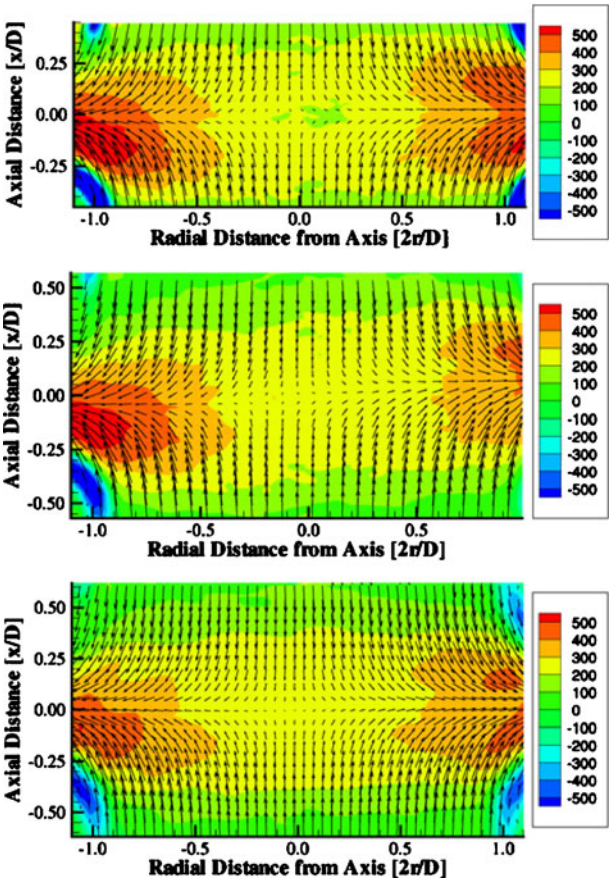

Fig. 19 Contours of mean radial strain overlaid with the velocity vectors at $U_b = 4.0$ m/s and increasing nozzle separation. H/D: (*top*) 1.0, (*middle*) 1.2 and (*bottom*) 1.4

comparison of PIV data, obtained using a medium resolution ($L = 4.6l_t$, $L_w = 0.33$), hot-wire measurements and the standard model by Pope [36] is presented in Fig. 16. Reasonably good agreement for the PIV derived energy spectrum was found for wavenumbers between 10^2 to 10^3. To resolve the energy spectrum for a wavenumber range between 20 and $5 \cdot 10^3$, a domain length of ten times the integral length scale and a resolution of the order of the Kolmogorov length scale would be required.

3.3 Strain rates

The definitions of bulk (a_b), axial (a_{ax}) and radial (a_{rad}) rates of strain are given in (8) and mean radial strain rates for the current axi-symmetric geometry along the stagnation plane are presented in Fig. 18 for nozzle separations H/D = 1.0 and 1.4 for bulk velocities of 4.0 and 8.0 m/s.

$$a_b = 2\frac{U_b}{H}; \qquad a_{ax} = \frac{\partial U}{\partial x}; \qquad a_{rad} = \frac{V}{r} + \frac{\partial V}{\partial r} \tag{8}$$

The radial strain rates have a minimum in the proximity of the stagnation point and increase towards the nozzle rim with values up to 500 s^{-1} for a bulk velocity of 4.0 m/s and 1,000 s^{-1} for 8.0 m/s. The maximum positional uncertainties for the nozzles with the current system are 0.2 mm for the coaxial alignment and 0.5° in the angular alignment. Despite the high accuracy in the concentric alignment of the nozzles, slight asymmetries in the radial strain rates can still be seen. The radial strain rates are of comparable magnitude to those previously reported by Lindstedt et al. [2].

Contour plots of the mean radial strain rates overlaid with velocity vectors for nozzle separations of H/D = 1.0, 1.2 and 1.4 are shown in Fig. 19. Peaks in the mean radial strain can be found at approximately 1.0D away from the nominal stagnation point. Again, the strain rates are broadly in agreement with previous work presented by Lindstedt et al. [2] and Korusoy and Whitelaw [35]. The asymmetry in the mean radial strain rates is due to a slight coaxial misalignment of the nozzles (≤ 0.2 mm).

4 Conclusions

A parametric study of turbulence generation in an opposed jet geometry has been performed using fractal grids with results compared to those obtained using conventional perforated plates. The work shows that fractal grids can increase turbulence levels by more than 100% at the nozzle exits. It was also shown, using a transparent nozzle, that 10 mm upstream of the nozzle exit nearly isotropic conditions prevailed while at a location of 3 mm downstream of the nozzle exit anisotropy was apparent. Hence, the current measurements provide information concerning the growth of anisotropy in the opposed jet configuration. The influence of variations of fractal grid parameters suggest that an increase of the smallest and largest fractal dimensions serve to increase the turbulence intensities. It was also found that a blockage of approximately 75% resulted in the highest turbulent intensities at the expense of less uniform radial fluctuations. Accordingly, a grid with a total area blockage of 65% was chosen for all further measurements. The observed flow non-uniformities outside the nozzle region are caused by the shear layer between the opposed flow and the co-flowing streams. For cases where the impact is of significant importance (e.g. combustion applications) the effect can be controlled by adjustments to the co-flow.

The low turbulence intensities produced by conventional perforated plates have been problematic in the opposed jet geometry. Lindstedt et al. [2] stated that the agreement between calculated Reynolds stress components and PIV-measurements improved considerably for Reynolds numbers above 10,000, but remained problematic at lower values. However, bulk strain rates at the higher Reynolds numbers caused early extinction for most fuel types while a reduction in the Reynolds number caused arguably too low turbulence levels for calculation methods based on the assumption of fully turbulent flows. The current addition of fractal grids was found to increase the turbulent Reynolds number range from 48–125 to 109–220 while maintaining the same bulk strain contribution. The implications for combusting flows will be explored in future work.

The movement of the instantaneous stagnation point was quantified and probability density functions showed an axial movement of up to 4 mm with an associated radial movement of 2 mm. Two different data processing algorithms were developed and tested with the aim of identifying the instantaneous location of the stagnation point. It was shown that an area based search algorithm needs to be used as line algorithms fail to trace the location whenever the stagnation point moves in the radial direction or if there is a large scale eddy present along the centreline of the burner. The implications for velocity statistics of including the low frequency bulk motion was also assessed. While the radial statistics remain broadly unaffected, the axial turbulence values should be treated as upper limit values with a potential uncertainty of the order 20%. The fact that the flow in the stagnation point region is influenced by bulk movement will exert an influence on the characteristics of turbulent flames in the opposed jet geometry. Accordingly, significant care is required in terms of the analysis and procurement of data for such flames, in particular for cases close to extinction where the inclination of the flame surface may be strongly time dependent.

Acknowledgements The current work was carried out with the financial support of the US Office of Naval Research under grant N00014-07-1-0993. The support of Dr Gabriel Roy, Dr Robert Barlow and Prof Andreas Dreizler is gratefully acknowledged. The authors also wish to thank the Royal College of Art for manufacturing the fractal grids.

References

1. Craft, T.J., Launder, B.E., Suga, K.: Development and application of a cubic eddy-viscosity model of turbulence. Int. Heat J. Fluid Flow **17**, 108–115 (1996)
2. Lindstedt, R.P., Luff, D., Whitelaw, J.H.: Velocity and strain-rate characteristics of opposed isothermal flows. Flow Turbul. Combust. **74**, 169–194 (2005)
3. Kempf, A., Forkel, H., Sadiki, A., Janicka, J., Chen, J.-Y.: Large eddy simulation of counterflow configuration with and without combustion. Proc. Combust. Inst. **28**, 35–40 (2000)
4. Yakhot, V., Orzag, A., Thangam, S., Gatski, T.B., Speziale, C.G.: Development of turbulence models for shear flows by a double expansion technique. Phys. Fluids **4**, 1510–1520 (1992)
5. Haworth, D.C., Pope, S.B.: A generalized langevin model for turbulent flows. Phys. Fluids **29**, 387–405 (1986)
6. Haworth, D.C., Pope, S.B.: A pdf modeling study of self-similar turbulent free shear flows. Phys. Fluids **30**, 1026–1044 (1987)
7. Geyer, D., Kempf, A., Dreizler, A., Janicka, J.: Turbulent opposed-jet flames: a critical benchmark experiment for combustion LES. Combust. Flame **143**, 524–548 (2005)
8. Bray, K.N.C., Champion, M., Libby, P.A.: Premixed flames in stagnating turbulence part II—the mean velocities and pressure and the Damköhler number. Combust. Flame **112**, 635–654 (1998)
9. Rolon, J.C., Veynante, D., Martin, J.P.: Counter jet stagnation flows. Exp. Fluids **11**, 313–324 (1991)

10. Mastorakos, E., Taylor, A.M.K.P., Whitelaw, J.H.: Scalar dissipation rate at the extinction of turbulent counterflow nonpremixed flames. Combust. Flame **91**, 55–64 (1992)
11. Kostiuk, L.W., Bray, K.N.C., Cheng, R.K.: Experimental study of premixed turbulent combustion in opposed streams. Part I—nonreacting flow field. Combust. Flame **92**, 377–395 (1993)
12. Mounaïm-Rousselle, C., Gökalp, I.: Turbulent premixed combustion in counterflow geometry. The influence of a coflow. In: Spring Annual Meeting of the Western States Section of the Combustion Institute (1993)
13. Sardi, K., Taylor, A.M.K.P., Whitelaw, J.H.: Conditional scalar dissipation statistics in a turbulent counterflow. Fluid J. Mech. **361**, 1–24 (1998)
14. Stan, G., Johnson, D.A.: Experimental and numerical analysis of turbulent opposed impinging jets. AIAA J. **39**(10), 1901–1908 (2001)
15. Geyer, D., Omar, S., Nauert, A., Ludwig, A., Dreizler, A., Janicka, J.: A comprehensive characterisation of a turbulent opposed jet flame by 1D-Raman/Rayleigh, 2D-LIF and 2D-LDV. VDI-Ber. **1750**, 435–440 (2003)
16. Coppola, G., Coriton, B., Gomez, A.: Highly turbulent counterflow flames: a laboratory scale benchmark for practical systems. Combust. Flame **156**, 1834–1843 (2009)
17. Korusoy, E., Whitelaw, J.H.: Extinction and relight in opposed flames. Exp. Fluids **33**, 75–89 (2002)
18. Mastorakos, E.: Turbulent combustion in opposed jet flows. Ph.D. thesis, Imperial College London, UK (1993)
19. Kostiuk, L.W., Bray, K.N.C., Cheng, R.K.: Experimental study of premixed turbulent combustion in opposed streams. Part II—reacting flow field and extinction. Combust. Flame **92**, 396–409 (1993)
20. Hurst, D., Vassilicos, J.C.: Scaling and decay of fractal-generated turbulence. Phys. Fluids **19**(035103), 1–31 (2007)
21. Seoud, R.E.,Vassilicos, J.C.: Dissipation and decay of fractal generated turbulence. Phys. Fluids **19**(105108), 1–11 (2007)
22. Vassilicos, J.C., Hunt, J.C.R.: Fractal dimensions and spectra of interfaces with application to turbulence. Proc. Roy. Soc. A **435**(1895), 505–534 (1991)
23. Lindstedt, R.P., Luff, D.S.: Velocity fields of lean premixed turbulent opposed jet flames. Proc. Combust. Inst. **31**, 1459–1466 (2007)
24. Kostiuk, L.W., Shepherd, I.G., Bray, K.N.C.: Experimental study of premixed turbulent combustion in opposed streams. Part III—spatial structure of flames. Combust. Flame **118**, 129–139 (1999)
25. Mastorakos, E., Taylor, A.M.K.P., Whitelaw, J.H.: Extinction of turbulent counterflow flames with reactants diluted by hot products. Combust. Flame **102**, 101–114 (1995)
26. Sardi, K., Whitelaw, J.H.: Extinction timescales of periodically strained, lean counterflow flames. Exp. Fluids **27**, 199–209 (1999)
27. Mastorakos, E., Taylor, A.M.K.P., Whitelaw, J.H.: Extinction and temperature characteristics of turbulent counterflow diffusion flames with partial premixing. Combust. Flame **91**, 40–54 (1992)
28. Sardi, K., Taylor, A.M.K.P., Whitelaw, J.H.: Extinction of turbulent counterflow flames under periodic strain. Combust. Flame **120**, 265–284 (2000)
29. Luff, D.S.: Experiments and calculations of opposed and ducted flows. Ph.D. thesis, Imperial College London, UK (2005)
30. Kostiuk, L.W.: Premixed turbulent combustion in counterflowing streams. Ph.D. thesis, Churchill College, University of Cambridge (1991)
31. Han, D., Mungal, M.G.: Simultaneous velocity and CH distributions. Part I: Jet flames in a co–flow. Combust. Flame **132**, 565–590 (2003)
32. Denshchikov, V.A., Kontratev, V.N., Romashev, A.N.: Interaction between two opposed jets. Fluid Dyn. **13**(6), 313–324 (1978)
33. Denshchikov, V.A., Kontratev, V.N., Romashev, A.N., Chubarov, V.M.: Auto-oscillation of planar colliding jets. Fluid Dyn. **18**(3), 460–462 (1978)
34. Mounaïm-Rousselle, C., Gökalp, I.: Strain effects on the structure of counterflowing turbulent premixed flames. Proc. Combust. Inst. **25**, 1199–1205 (1994)
35. Korusoy, E., Whitelaw, J.H.: Opposed jets with small separations and their implications for the extinction of opposed flames. Exp. Fluids **31**, 111–117 (2001)
36. Pope, S.B.: Turbulent Flows. Cambridge University Press, Cambridge, UK (2000)
37. von K*ármán*, T.: Progress in the statistical theory of turbulence. Proc. Natl. Acad. Sci. USA **34**, 530–539 (1948)

38. Kraichnan, R.H.: The structure of isotropic turbulence at very high Reynolds numbers. J. Fluid Mech. **5**, 497–543 (1959)
39. Pao, Y.-H.: Structure of turbulent velocity and scalar fields at large wavenumbers. Phys. Fluids **8**, 1063–1075 (1965)
40. Comte-Bellot, G., Corrsin, S.: Simple Eulerian time correlation of full- and narrow-band velocity signals in grid-generated, isotropic turbulence. J. Fluid Mech. **48**(02), 273–337 (1971)